JOURNAL OF COMPUTATIONAL PHYSICS 122, 96–106 (1995)

A Fully Conservative Interface Algorithm for Overlapped Grids

Z. J. WANG

CFD Research Corporation, 3325 Triana Boulevard, Huntsville, Alabama 35805

Received July 26, 1994; revised April 28, 1995

A fully conservative zonal interface algorithm has been developed for overlapped (Chimera) grids. In this new approach, overlapped zones are transformed into patched zones. Flux conservation is then enforced on the patch boundary in a local sense, thus guaranteeing global conservation. This algorithm also unifies the interface treatment for patched and overlapped grids. The zonal interface scheme has been successfully implemented into a cell-centered finite volume code. Test cases indicated that the newly developed interface scheme is indeed fully conservative, highly accurate, and possesses superior convergence properties when compared to the original Chimera scheme. © 1995 Academic Press, Inc.

1. INTRODUCTION

To handle complex geometries and flow physics in computational fluid dynamics (CFD) analysis, a multizonal approach is highly favored over the single-zonal approach. In the multizonal (multiblock) approach, the flow domain is divided into a number of geometrically simple subdomains (zones) in which independent meshes can be generated and different flow physics (governing equations) can be applied if necessary. The multizonal approach also has the advantage that the mesh in a certain zone of the flow domain can be easily refined to accurately resolve complex flow features (shock waves, slip lines, vortices, etc.) without modifying the meshes in the neighboring zones. Furthermore, multizonal algorithms can be easily adapted to take advantage of multiprocessor parallel computers.

There are two different multizonal approaches depending on whether zonal boundaries exactly match or arbitrarily intersect each other. The former is named Patched grid approach and the latter the Overlapped (Chimera) grid approach. Both grid topologies are shown in Fig. 1.

A systematic study on the cell-vertex based (finite difference) patched grid approach was carried out by Rai [1, 2], who proposed a conservative zonal scheme and later extended it to an implicit relaxation algorithm for Euler equations. Its extension to three-dimensional viscous flow and to cell-center based finite volume schemes were reported by Walters *et al.* [3] and Klopfer *et al.* [4]. The major drawback of the patched grid scheme is the limitation of the exact match that it imposes on zonal interfaces.

In addition to the patched grid approach, another strategy, namely overlapped grid based multizone approach, was under development. The most extensive and noticeable work of overlapped grid is the so-called Chimera method developed by Benek *et al.* [5] and further extended by Steger *et al.* [6] and Benek *et al.* [7]. More recently, the Chimera grid scheme was applied to complex three-dimensional unsteady problems such as separation of the spacecraft orbiter from the boosters [8]. Since interpolations are used between grids to exchange information in the Chimera grid scheme, the overlapped grid approach is intrinsically nonconservative and, thus, has had difficulty and uncertainty in capturing shock waves. It was also reported in [9] that the convergence rate of a steady problem might depend on the overlapped region, and in some cases convergence could not be achieved. Although some improvement on the conservation properties of the Chimera were proposed by several researchers, e.g., Moon *et al.* [10], the results were not fully satisfactory. A conservative constraint was employed in [10]; however, the condition used was not sufficient to guarantee conservation.

Some advantages and disadvantages of the previous patched and overlapped grid algorithms are summarized below

a. patched grid scheme
   - fully conservative
   - interpolation from one zone to another zone is unnecessary (for cell-centered based finite volume schemes), but
   - zonal interfaces need perfect match;

b. overlapped grid scheme
   - arbitrary boundary interface matches
   - grids can move relative to each other easily, but
   - zonal boundary treatment is not fully conservative
   - two-way interpolations are required.

Due to the nonlinear nature of Euler equations, care needs to be taken when they are solved in a discretized manner. It is well known that given a smooth initial condition, discontinuities may develop in the solution due to the hyperbolic nature of these equations. Capturing the discontinuities in the Euler solutions was one of the challenges faced by applied mathematicians during the early stages of CFD development. Lax [11] established several criteria which guarantee that the numerical solu-

0021-9991/95 $12.00

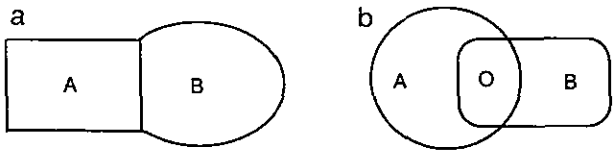

FIG. 1. Two types of multizonal grid approaches.

tion is indeed the physically relevant weak solution to the Euler equations in one of his most famous papers. These criteria can be summarized as: conservation and the entropy condition (besides consistency and stability). Since most numerical schemes are dissipative, the entropy condition is usually satisfied. Therefore, the other criterion of the numerical scheme is conservation. Fortunately, most CFD numerical algorithms used today are conservative. However, the use of multizonal grid approaches introduces artificial boundaries into the physical domain, i.e., zonal interfaces. It is important that these interfaces are treated conservatively to guarantee global conservation. Otherwise, although the numerical scheme is *zonally* conservative it is nonconservative *globally*.

Because of the difficulty in treating the interface of overlapped grids conservatively, nonconservative interpolations were used in practice to exchange information between overlapped zones. The effects of this globally nonconservative scheme to the overall solution accuracy have not been understood. With a globally conservative numerical scheme, one can be *sure* the physically relevant numerical solution will be obtained (in the limit of global grid refinement). However, it is uncertain that one will *always* obtain the correct physical solution with a nonconservative numerical scheme. Until it is proved otherwise, the uncertainty will always be there.

The current study addresses the very root of the problem—conservative interface treatment for overlapped grids. The new interface scheme will be shown to be fundamentally conservative. With a globally conservative numerical scheme, one can apply Chimera to previously unexplored flow problems with confidence.

2. CONDITIONS OF CONSERVATION

Consider the following conservation laws written in integral form:

$$\int_V \frac{\partial Q}{\partial t}\, dV + \oint_S F\, dS = 0. \tag{1}$$

The vectors Q and F are given by

$$Q = \begin{Bmatrix} \rho \\ \rho u \\ \rho v \\ \rho w \\ e \end{Bmatrix}, \quad F = \begin{Bmatrix} \rho v_n \\ \rho u v_n + p n_x \\ \rho v v_n + p n_y \\ \rho w v_n + p n_z \\ (e+p) v_n \end{Bmatrix}, \tag{2}$$

where ρ, p, e and u, v, w are density, pressure, total energy, and Cartesian velocity components, respectively, $\mathbf{n} = (n_x, n_y, n_z)$ is the unit normal of the surface, S, and $v_n = \mathbf{v} \cdot \mathbf{n}$. Pressure, p, is related to the total energy, e, by the ideal gas law,

$$p = (\gamma - 1)\left(e - \frac{\rho}{2}|v|^2\right). \tag{3}$$

In a finite-volume approach the physical domain is further divided into small cells called control volumes. Let a semi-discrete numerical scheme for a control volume ΔV in V be written as

$$\frac{\partial Q}{\partial t}\Delta V = -\sum_f F_f\, dS_f, \tag{4}$$

where Q now represents the cell-averaged conservative variables and the summation index f denotes all surrounding faces of ΔV. Scheme (4) is conservative in V if it satisfies

$$\sum_{\Delta V \in V} \frac{\partial Q}{\partial t}\Delta V = -\sum_{f \in \Gamma} F_f\, dS_f, \tag{5}$$

where Γ is the boundary of the physical domain V.

Now consider two general overlapping zones A and B shown in Fig. 1b and assume conservative schemes are used in both regions; then

$$\sum_{\Delta V \in A} \frac{\partial Q_A}{\partial t}\Delta V = -\sum_{f \in \Gamma_A} F_f\, dS_f \tag{6}$$

$$\sum_{\Delta V \in B} \frac{\partial Q_B}{\partial t}\Delta V = -\sum_{f \in \Gamma_B} F_f\, dS_f. \tag{7}$$

Where Γ_A and Γ_B are the boundaries of A and B. Let O be the overlapping region between region A and B, i.e., $O = A \cap B$ and let G be the global domain formed by A and B, i.e., $G = A \cup B$. Since only unique physical variables are possible in region O, the following physical condition should be satisfied:

$$\sum_{\Delta V \in O} \frac{\partial Q_B}{\partial t}\Delta V = \sum_{\Delta V \in O} \frac{\partial Q_A}{\partial t}\Delta V. \tag{8}$$

A conservative scheme for the global domain G must satisfy

$$\sum_{\Delta V \in G} \frac{\partial Q}{\partial t}\Delta V = \sum_{f \in \Gamma_G} F_f\, dS_f. \tag{9}$$

It is obvious that

$$\Gamma_G = \Gamma_A + \Gamma_B - \Gamma_{AO} - \Gamma_{BO},$$

where Γ_{BO} is part of the boundary of B which is overlapped by A, and Γ_{AO} is defined similarly. From Eqs. (6)–(9), the following conservative condition is obtained:

$$\sum_{\Delta V \in O} \frac{\partial Q}{\partial t} \Delta V = \sum_{f \in -\Gamma_{AO} - \Gamma_{BO}} F_f \, dS_f. \tag{10}$$

Since Equations (6)–(9) are necessary and sufficient conditions of conservation, (10) is also a necessary and sufficient condition of conservation for the overlapping regions. If two regions are patched together, then the necessary and sufficient condition is the conservation of total flux along the common boundary, i.e.,

$$\sum_{f \in \Gamma_{AO}} F_f \, dS_f = -\sum_{f \in \Gamma_{BO}} F_f \, dS_f. \tag{11}$$

3. A CONSERVATIVE INTERFACE ALGORITHM

The two conditions given in (8) and (10) are necessary and sufficient conditions of conservation for general overlapped zones. Its implementation is extremely difficult due to the following reasons:

- two new internal boundaries (Γ_{AO} in B and Γ_{BO} in A) need to be generated to enforce these conditions; and
- the simultaneous enforcement of both (8) and (10) is extremely difficult, if not impossible.

In fact, only condition (8) is enforced in 2D in [10]. Its extension to 3D involves very complex volume integration and is almost impossible to implement. Another condition of conservation is given in [12]. Its implementation is unknown.

In this study, a new approach is developed. The basic idea is very simple, i.e., to transform two overlapped zones into two patched zones by taking advantage of one of the overlapping boundaries, e.g., Γ_{BO} in Fig. 2. Γ_{BO} becomes a patch boundary (PB) between zone (A-O) and B. The condition of conservation is now flux conservation along the common patch boundary Γ_{BO} (see Eq. (11)). One key step in this approach is the generation of a new zonal interface within zone A. Key advantages of the present approaches are:

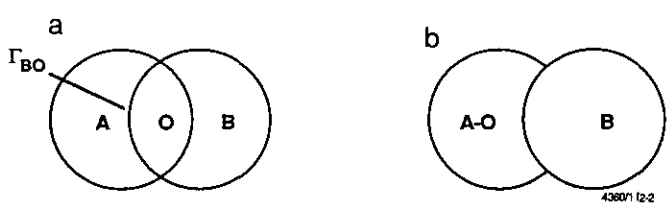

FIG. 2. Transformation of overlapped zones to patched zones.

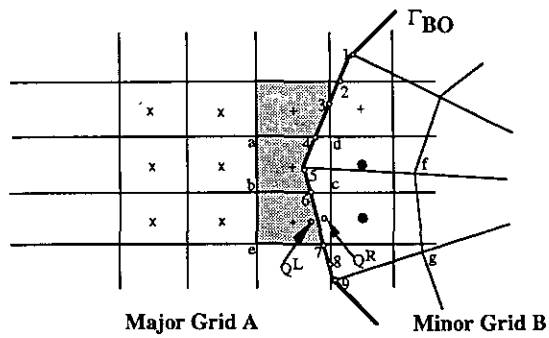

FIG. 3. Schematic of conservative treatment of overlapped grid interface.

1. Conservative;
2. Unique solution in region O; and
3. Interpolations between zones unnecessary.

Details of the approach are given below.

3.1. *Zonal Interface Generation (ZIG)*

To enforce flux conservation, it is necessary to generate a new internal boundary Γ_{BO} within zone A (major grid) to enforce the conservation condition. Let us refer to Fig. 3. The representation of Γ_{BO} in 2D is joined line segments, e.g., 1–5, 5–9, etc. These line segments intersect with cell faces of grid A. These cell faces which are intersected by Γ_{BO} are named cut faces (CF), e.g., b-6, a-4. It is obvious that boundary segments of grid B (minor grid) are further cut into even smaller segments by CF. For example, segment 1–5 is cut into 1–2, 2–3, 3–4, and 4–5. These smaller segments are named smallest faces (SF). By conserving flux (mass, momentum, energy) on the SF in the local sense, global conservation is guaranteed.

Three different types of cells are generated in grid A due to the appearance of the new internal boundary Γ_{BO}:

Cut cells (CC). Cells in the major grid that are cut by Γ_{BO}, i.e., cells with "+"

Normal cells (NC). Cells in the major grid that are outside the region covered by the minor grid, i.e., cells marked with "x"

Hole cells (HC). Cells in the major grid that are inside the region covered by the minor grid, i.e., cells marked with "•".

It is observed that flow variables in NC can be updated straightforwardly using information from surrounding cells, while HC are excluded from the computational domain. To updated flow variables in CC, fluxes on SF and CF need to be available. In addition, geometric quantities such as the area vectors of SF and CF and the volume of CC need to be determined. ZIG involves determining all the relevant area vectors and volumes.

3.2. *Flux Calculation on the Patch Boundary*

Since the patch boundary Γ_{BO} is composed of SF, fluxes on each smallest face need to be calculated. Two separate steps

are taken to obtain the fluxes: reconstruction and the Riemann solver:

Reconstruction. Referring to Fig. 3, to calculate flux on the smallest face, 6–7, cell-wise reconstructions are carried out at cell *b*67*e* and cell 59*gf* to calculate the flow variables just to the left and right of the face, Q^L and Q^R. Both cell-wise constant and cell-wise linear reconstructions can be used. Cell-wise constant reconstruction results in a first-order interface scheme while cell-wise linear reconstruction gives a second-order interface treatment. For a cell-wise constant reconstruction, Q^L is simply the flow variable at the cell center of *b*67*e* and Q^R is the variable at the center of cell 59*gf*.

For cell-wise linear reconstruction, neighboring cells are used to construct the gradients. Using the Taylor expansion with respect to the cell center up to first order we obtain

$$q_{x,y} = q_{xo,yo} + \frac{\partial q}{\partial x}(x - x_0) + \frac{\partial q}{\partial y}(y - y_0), \tag{12}$$

where q represents the primitive variables. For each neighboring cell, we have one equation like (12). Then these equations are solved in a least square sense to get the gradients ($\partial q/\partial x$, $\partial q/\partial y$). Next the gradients are used to calculate Q^L and Q^R based on the position vector at the center of face 6–7.

Riemann solver. Roe's Riemann solver [13] is used to make the interface scheme compatible with the interior discretization. The flux is determined given the left and right state vectors, as well as the face normal vector, i.e.,

$$F_f = F(Q_f^L, Q_f^R, n). \tag{13}$$

3.3. *Updating of Flow Variables*

After the flux along the common patching boundary Γ_{BO} is decided, it is straightforward to update the conservative variables in the minor grid B. For example, flux through face 1–5 can be summed from fluxes through 1–2, 2–3, 3–4, and 4–5.

The approach to update the conservative variables in cut cell of grid A is described next. For any cut cell, the flux through the boundary of the cell can generally be expressed as

$$\begin{aligned}\sum_{f\in\Gamma_{cc}} F_f = {} & F_{i+1/2,j}W_{i+1/2,j} - F_{i-1/2,j}W_{i-1/2,j} \\ & + F_{i,j+1/2}W_{i,j+1/2} - F_{i,j-1/2}W_{i,j-1/2} + \Sigma F_{SF},\end{aligned} \tag{14}$$

where $F_{i+1/2,j}$ etc. are fluxes through the cut cell which are calculated in the "normal" way, $W_{i+1/2,j}$ etc. are area weights for the corresponding cut cell, and F_{SF} is the flux through the SF within the cut cell. Some examples of the weights are given in Fig. 4. With this treatment, the fluxes through all the cut cells can be cast in the same form no matter what shapes they happen to be in. After the fluxes are calculated, the conservative variables of the cut cell can be updated directly.

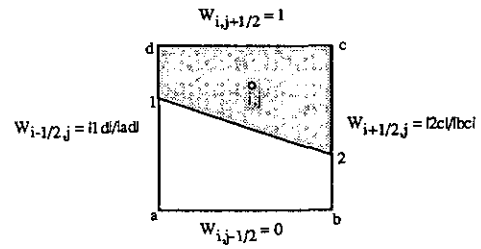

FIG. 4. Examples of weights for irregular polygonal control volumes.

4. FLOW SOLVER

The flow solver is based on a cell-centered finite volume discretization. If Eq. (1) is integrated in a control volume, as found in a structured grid, then

$$\Delta V\frac{\partial Q}{\partial t} + \sum_{f=1}^{N} F_f = 0, \tag{15}$$

where N is number of faces surrounding ΔV. The inviscid flux in Eq. (15) is calculated using the MUSCL reconstruction [14] and Roe's flux difference splitting [13]. The time integration is fulfilled by a fully implicit scheme with a Jacobian solver.

4.1. *Reconstruction*

Consider reconstruction in the i direction. We utilize a linear distribution (interpolation) of the solution ($q = \rho, u, v, w, p$),

$$q(\xi) = q_i + s_i(\xi - \xi_i), \quad \xi_{i-1/2} \le \xi \le \xi_{i-1/2}, \tag{16}$$

where ξ represent the arc length in the i-direction, s_i is the slope of the solution for cell i. If the slope is so defined that a monotonic profile is preserved, the scheme will produce no numerical oscillations. From Eq. (16) one may find the left and right flow properties at interface $i + 1/2$ to be

$$q_{i+1/2}^R = q_{i+1} - \tfrac{1}{2}s_{i+1}(\xi_{i+3/2} - \xi_{i+1/2}) \tag{17}$$

$$q_{i+1/2}^L = q_i + \tfrac{1}{2}s_i(\xi_{i+1/2} - \xi_{i-1/2}). \tag{18}$$

The slope function can be expressed as

$$s_i = \varphi(r_i)\frac{q_i - q_{i-1}}{\xi_i - \xi_{i-1}}, \tag{19}$$

$$r_i = \frac{(q_{i+1} - q_i)(\xi_i - \xi_{i-1})}{(q_i - q_{i-1})(\xi_{i+1} - \xi_i)}, \tag{20}$$

and $\varphi(r)$ is the so-called minmod limiter,

$$\varphi(r) = \max(0, \min(1, r)) \tag{21}$$

4.2. *Riemann Solver*

After the flow variables to the left and right of a face Q^L and Q^R are known, Roe's approximate Riemann solver is used to compute the numerical flux. The flux of face f takes the same form as (13).

4.3. *Time Integration*

After spatial discretization, the equation to be integrated in time is (15). In the present study, primitive variables $q = (\rho, u, v, w, p)^T$ are updated. Equation (15) can be rewritten as

$$\Delta V M \frac{\partial q}{\partial t} = -\sum_f F_f, \tag{22}$$

where

$$M = \frac{\partial Q}{\partial q} = \begin{Bmatrix} 1 & 0 & 0 & 0 & 0 \\ u & \rho & 0 & 0 & 0 \\ v & 0 & \rho & 0 & 0 \\ w & 0 & 0 & \rho & 0 \\ \frac{1}{2}|v|^2 & \rho u & \rho v & \rho w & \frac{1}{\gamma - 1} \end{Bmatrix}.$$

If implicit backward Euler method is used for time discretization in (22), then

$$M \frac{q_i^{n+1} - q_i^n}{\Delta t} \Delta V + \sum_f F_f^{n+1} = 0 \tag{23}$$

or

$$M \frac{q_i^{n+1} - q_i^n}{\Delta t} \Delta V + \sum_f (F_f^{n+1} - F_f^n) = -\sum_f F_f^n. \tag{24}$$

Linearizing F_f^{n+1} with respect to F_f^n up to second order, we obtain

$$F_f^{n+1} = F_f^n + \frac{\partial F_f}{\partial q_i} \Delta q_i + \frac{\partial F_f}{\partial q_n} \Delta q_n, \tag{25}$$

where q_n is the primitive variable vector of the neighboring cell of i. Substituting Eq. (25) into Eq. (24), then

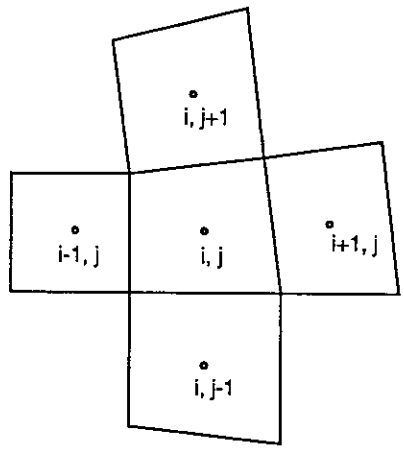

FIG. 5. The cell stencil for fully implicit scheme.

$$\left(\frac{\Delta V}{\Delta t} M + \sum_f \frac{\partial F_f}{\partial q_i}\right) \Delta q_i + \sum_f \frac{\partial F_f}{\partial q_n} \Delta q_n = -\sum_f F_f^n. \tag{26}$$

The stencil of the cells which are used to construct a fully implicit scheme at cell i is depicted in Fig. 5. This equation is then solved using a point Jacobian iterative solver, i.e.,

$$\left(\frac{\Delta V}{\Delta t} M + \sum_f \frac{\partial F_f}{\partial q_i}\right) \Delta q_i^{\theta+1} = -\sum_f F_f^n - \sum_f \frac{\partial F_f}{\partial q_n} \Delta q_n^\theta, \tag{27}$$

where θ represents an inner iteration number. The convergence of this inner iteration is controlled by the conditions,

$$|\Delta q_i^{\theta+1} - \Delta q_i^\theta| < \varepsilon \tag{28}$$

$$\theta + 1 < 0_{\max}, \tag{29}$$

where ε is a small positive tolerance number and $\theta_{\max}$ is a prescribed maximum inner iteration number.

5. NUMERICAL RESULTS

The conservative interface algorithm described in previous sections was implemented in a finite volume code, CFD-FASTRAN [15], which uses the algorithm described in the previous section. The criterion of freestream conserving was used to debug the code and has proved invaluable. To conserve a freestream, the area vectors of SF, CF need to be calculated correctly. The criterion was satisfied for every case performed in this study.

The main purpose of the test cases is to demonstrate the capability of the developed conservative interface scheme and to show the advantages it has over the nonconservative counterpart.

We have concentrated on the following aspects, which we

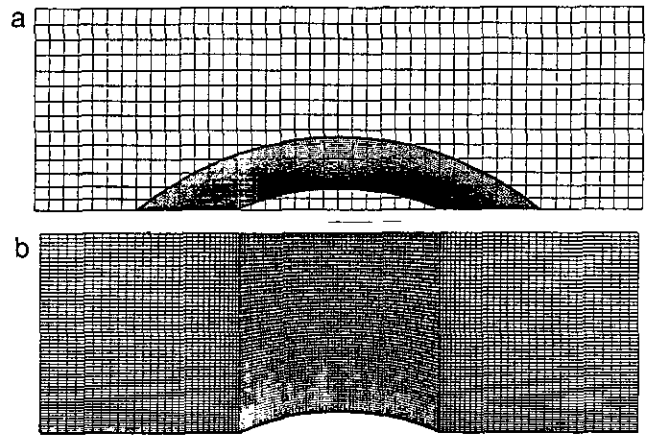

FIG. 6. Computational meshes used in transonic channel flow with 10% bump.

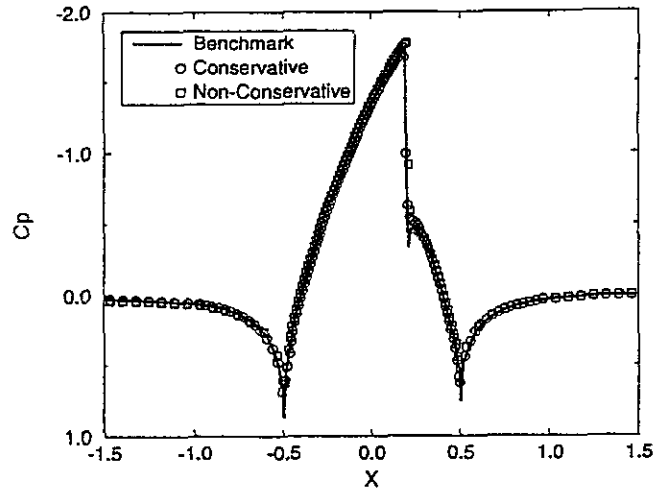

FIG. 8. Comparisons of Cp profiles on the lower wall of the channel.

believe a conservative scheme will distinguish itself from a nonconservative one:

a. correct strength and position of discontinuities;

b. net inflow or outflow mass must be zero for steady state calculations; and

c. convergence properties.

One may argue that the errors in conservative quantities are of the same order as the truncation error even if the scheme is nonconservative. This statement is true in theory. However, in regions near a discontinuity, derivatives of flow variables are infinite. The truncation error may be of second-order in theory at those regions, but it can be larger in magnitude than, say, a first-order error term in a smooth region. The large conservative error near the discontinuities can potentially result in shock waves with incorrect jump conditions or wrong locations even if the numerical scheme itself is of high-order in accuracy.

To compare the conservative Chimera (COC) with the original Chimera (ORC), a cell-centered finite volume code, CFL3D, from NASA Langley Research Center was used in this study besides CFD-FASTRAN. The ORC was implemented into CFL3D by Langley researchers. The reason for using CFL3D is that it is based on the same discretization schemes, such as cell-centered finite volume, MUSCL reconstruction with minmod limiter, and Roe's approximate Riemann solver. The difference between CFL3D and CFD-FASTRAN is in the time integration scheme. CFL3D employs a diagonized implicit operator, while CFD-FASTRAN uses a fully implicit scheme with a Jacobian solver. The difference in time integrations should disappear at steady state, which is affected only by the right-

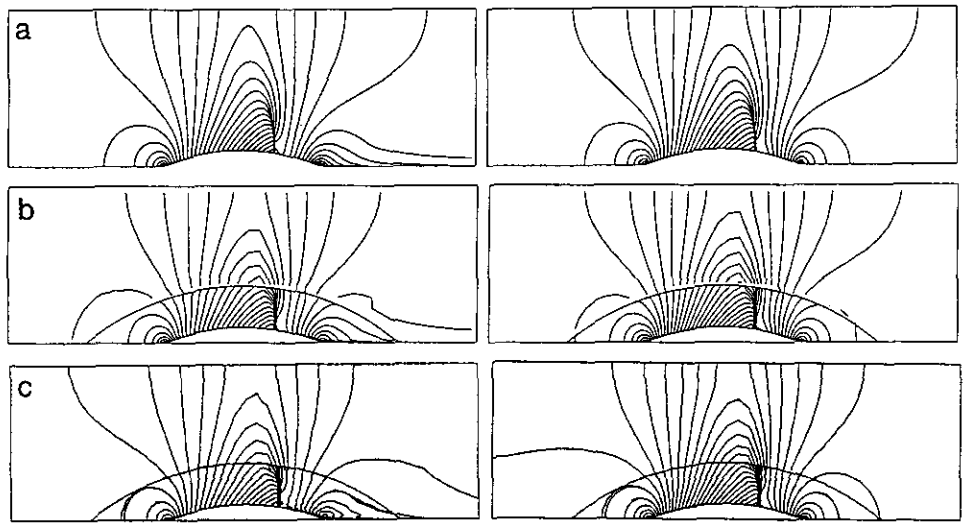

FIG. 7. Computed Mach and pressure contours for transonic channel flow.

TABLE I

Mass Flow Imbalance

	Inflow mass rate	Outflow mass rate	Imbalance
CFD-FASTRAN single zone	269.52534	269.52535	$4 \times 10^{-6}\%$
CFD-FASTRAN overlapped	269.47414	269.47412	$6 \times 10^{-6}\%$
CFL3D overlapped	269.8248	270.8508	0.38%

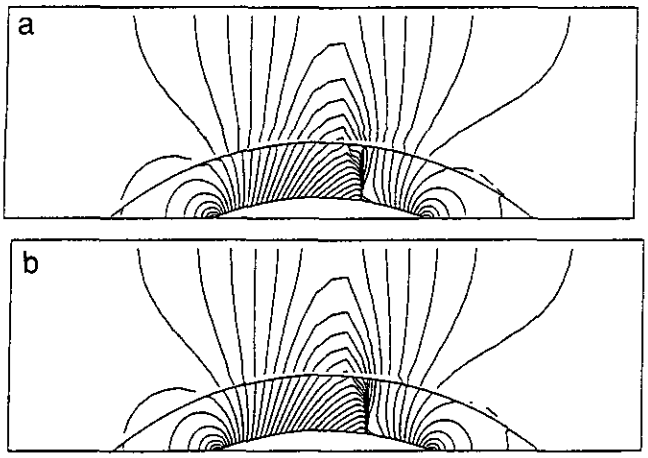

FIG. 9. Comparison of (a) zeroth-order and (b) first-order reconstruction at the patch boundary.

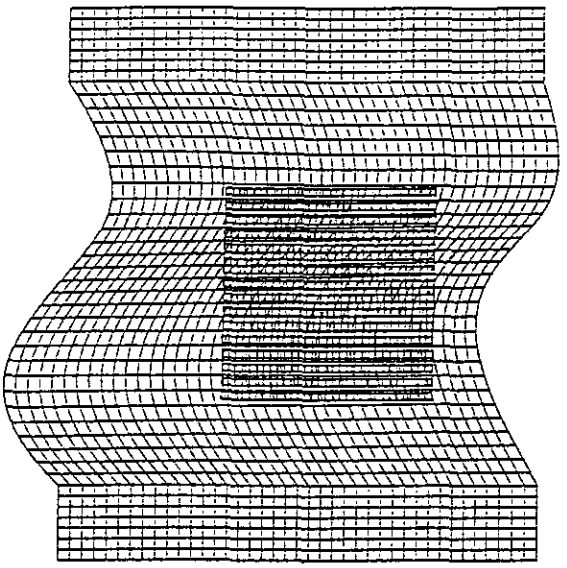

FIG. 11. Two-zone overlapped computational mesh used in moving shock problem.

hand side. Four 2D steady and unsteady cases will be presented in this section.

5.1. *Transonic Flow through a Channel with* 10% *Bump*

This case has been widely used to test compressible flow solvers in capturing shock waves. The width of the channel is equal to the length of the bump and the channel length is equal to three lengths of the bump. For the inlet Mach number of $M_{in} = 0.675$, a shock wave is generated over the bump. A two-zonal overlapped grid as shown in Fig. 6a was used in the simulations. The solution on a fine single-zonal grid, shown

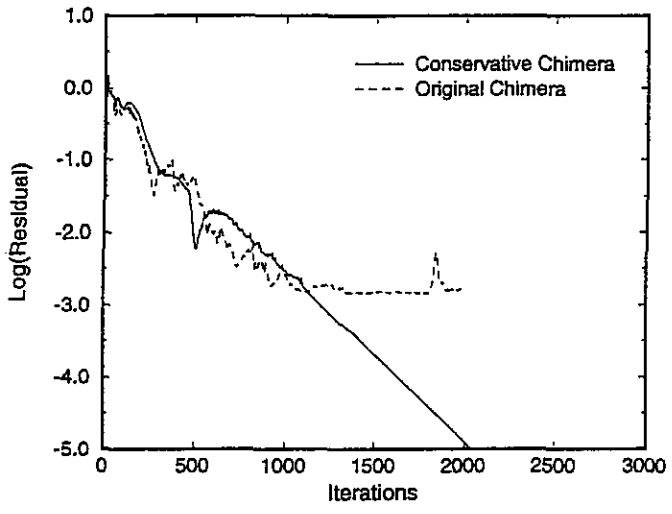

FIG. 10. Residual histories for transonic channel flow.

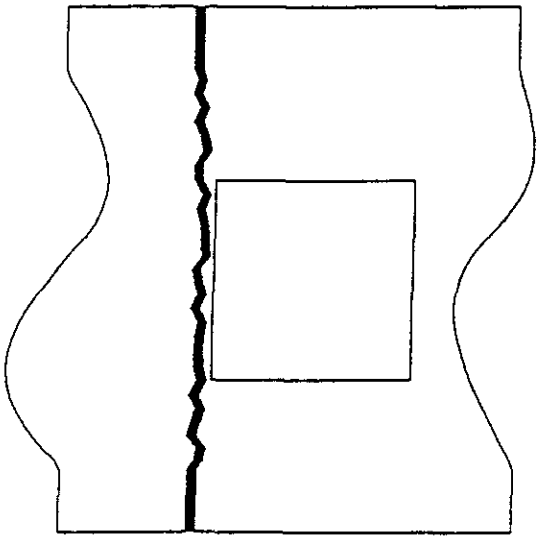

FIG. 12. The initial shock position at $t = 0$.

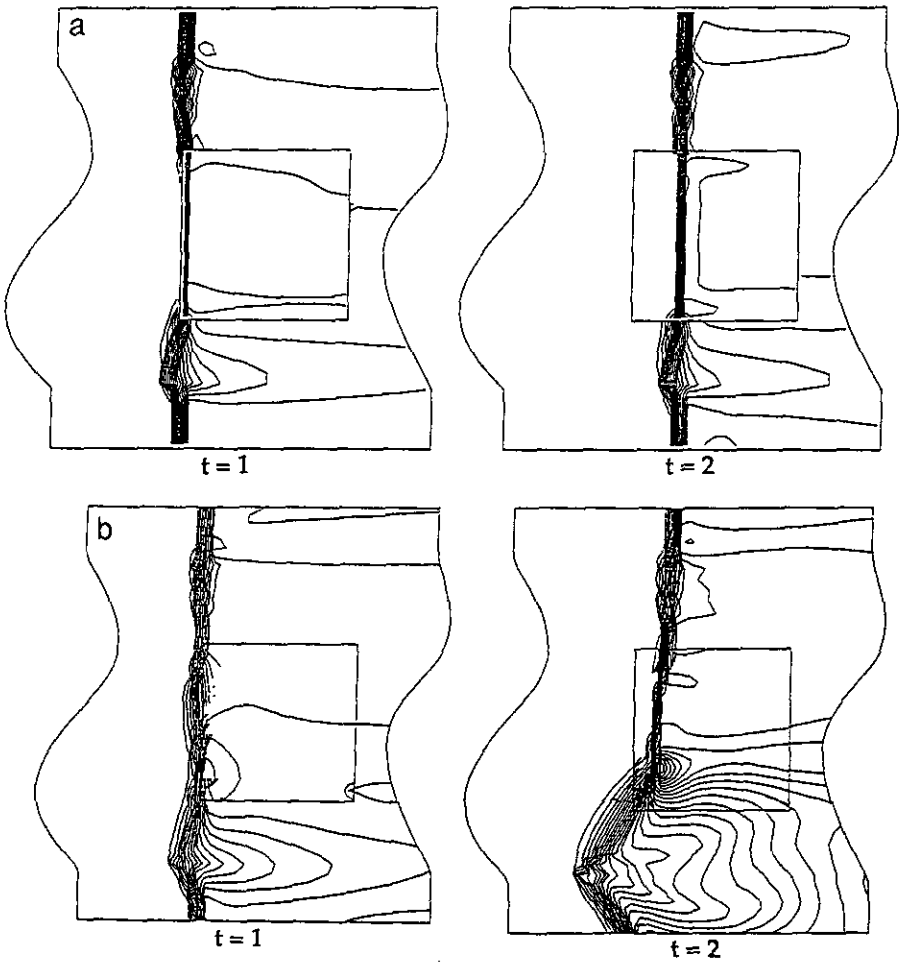

FIG. 13. Density contours for moving shock problem at $t = 1$ and $t = 2$.

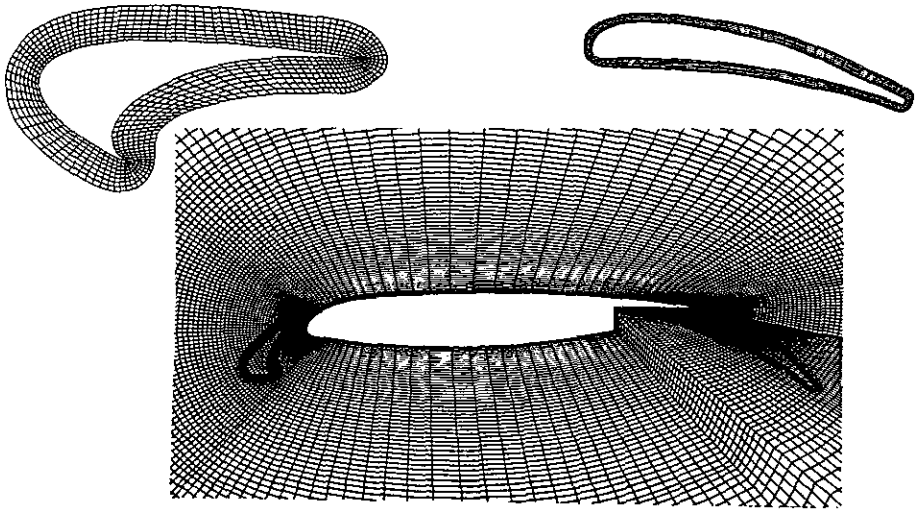

FIG. 14. Three zone Chimera grid for multielement airfoil flow.

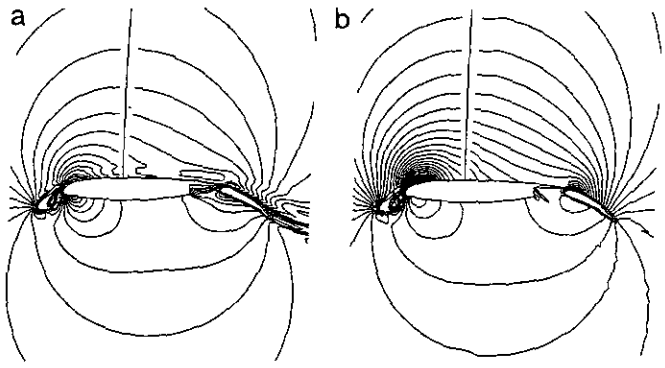

FIG. 15. Simulated Mach and pressure for multielement airfoil flow.

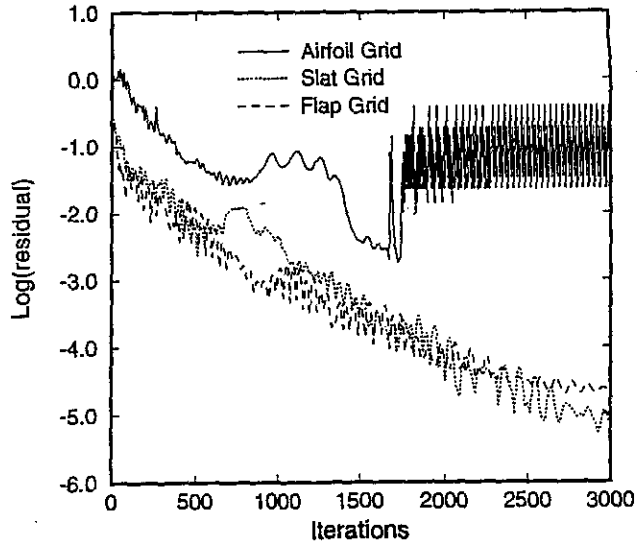

FIG. 17. Convergence histories for multielement airfoil flow.

in Fig. 6b, was used for comparison purposes. The two-zone Chimera grid was also used in simulation with CFL3D. Computed Mach and pressure contours are displayed in Fig. 7. Generally speaking, the contours calculated with the Chimera grids agree fairly well with the single-zone simulations. The same conclusions can be drawn with respect to the C_p distributions along the lower channel wall, which are shown in Fig. 8. However, there are large differences between these simulations in net mass imbalance, which is shown in Table I.

It can be observed that a machine-zero mass imbalance was achieved using COC in CFD-FASTRAN. The mass imbalance obtained with ORC in CFL3D was about five orders larger than that with CFD-FASTRAN. This clearly demonstrates the fully conservative nature of the COC.

A cell-wise constant reconstruction near the patch boundary was implemented to compare with a cell-wise linear reconstruction. Figure 9 shows the effects of the first-order and second-order zonal interface schemes. It is apparent that the second-order scheme delivers smoother variable transitions between the overlapped zones. Convergence histories of simulations with Chimera grids are displayed in Fig. 10. COC has no problem in converging to machine zero, while ORC stalled in convergence after several orders. The nonconservative interface treatment may have contributed to this convergence stall.

5.2. *Slow Moving Shock Problem*

Another classical test case for conservative and nonconservative schemes is the slow moving shock problem. It was demon-

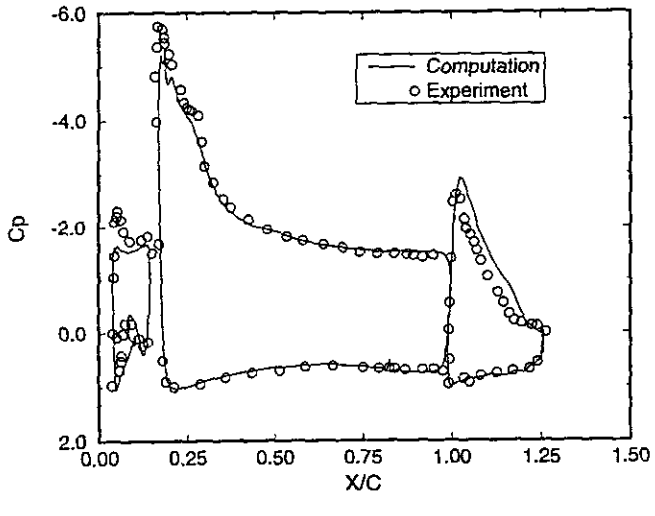

FIG. 16. Comparison of Cp profiles between computation and experiment.

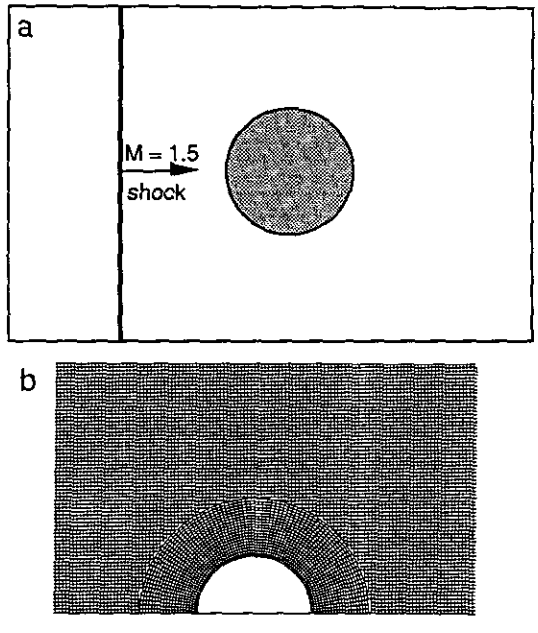

FIG. 18. Configuration and computational grids for shock diffraction by a cylinder.

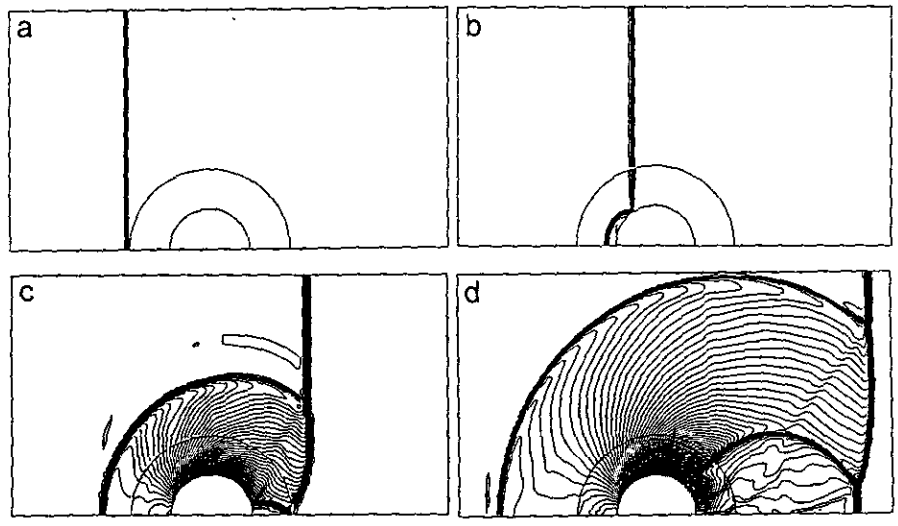

FIG. 19. Density contours at different times with Chimera grid.

strated by Part-Enander and Sjogreen [16] that a conservative interface scheme allowed a moving shock to pass through an overlapped interface, while a nonconservative scheme failed. The same problem was used in this study to see if COC performs any better than ORC. The pre- (left) and post-shock (right) flow conditions are: $\rho_l = 1.4$, $p_l = 1$, $u_l = 3$; $\rho_r = 5.38064$, $p_r = 10.2286$, and $u_r = 0.791673$. These conditions result in a shock moving from left to right in speed $v_s = 0.015$. A two-zone computational mesh, shown in Fig. 11 was used. At $t = 0$, the position of the shock is displayed in Fig. 12. At $t = 1$, 2, the density contours obtained by ORC and COC are shown in Fig. 13. It can be seen that some instabilities developed in the ORC calculation and caused the shock wave to dissipate and eventually disappear. The COC had no difficulty in resolving the moving shock wave and allowed the shock to pass through the interface.

5.3. *Three-Element Airfoil Flow*

The case of subsonic flow about a three-element airfoil was investigated experimentally by Valarezo *et al.* [17]. The flow conditions are: $M_\infty = 0.2$, $\alpha = 0.2°$, $Re = 9 \times 10^6$. In the present study, the inviscid flow assumption was made. The airfoil is composed of a slat, a main airfoil, and a trailing flap. It is an ideal case to demonstrate the geometric flexibility of Chimera. The three-zone overlapped grid is shown in Fig. 14. The mesh sizes are 85×7 for the slat, 209×79 for the main airfoil, and 136×9 for the flap. The outer boundary is placed 10 chord lengths away from the airfoil. The calculated pressure and Mach number contours are displayed in Fig. 15. The Cp distributions are compared with experimental data in Fig. 16. The agreement is generally fairly good, considering no viscous effects were included. The convergence history is shown in Fig. 17. Convergence stalled for the main airfoil after 1500 iterations. Careful examination of the flow field revealed that the flow near the leading edge of the main airfoil tended to separate and caused some limit-cycle-like oscillations. This may be due to negligence of viscous effects, since the flow was physically turbulent.

5.4. *Shock Diffraction by a Cylinder*

This unsteady test case is selected to test the Chimera algorithm in handling problems with strong nonlinear wave interactions. The definition of the problem and the computational mesh are shown in Fig. 18. An experimental shadowgraph is available to compare with numerical results. The density contours at various instants are displayed in Fig. 19. It is noticed that shock waves and slip lines can freely pass through and propagate along the overlapped zonal interface. Figure 20 compares the density contours of the present simulations with one shadowgraph picture from the experiment. There is very good agreement between numerical simulations and the experiment in overall features of the flow field—the shock waves, the slip lines, etc.

6. CONCLUSIONS

A fully conservative interface algorithm for overlapped Chimera grids has been developed. The algorithm was successfully implemented into a cell-centered finite volume code. In 2D, zonal interface generation (ZIG) takes about the same order of cpu time as one step of the flow solver. In 3D, ZIG is expected to be much more time-consuming. However, ZIG is carried out only once for nonmoving grids so the cost is negligible. At each iteration, fluxes need to be calculated on all smallest faces. This is the only overhead associated with the algorithm. This overhead is very small (<5% of total cpu) in comparison with the flow solver.

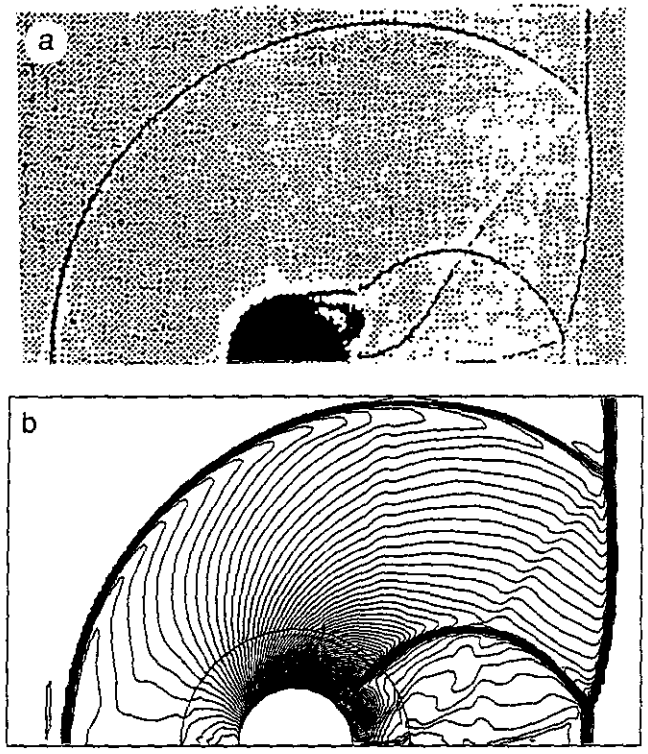

FIG. 20. Comparison of experiment shadowgraph with computational density contours.

Comparisons with the original (nonconservative) Chimera were carried out. Based on the study, the following conclusions can be made:

a. The present interface scheme for Chimera grids has been mathematically shown and numerically verified to be conservative. Zero mass imbalance was achieved up to machine accuracy for steady flows. Captured shock waves with the interface scheme showed excellent agreement with conservative single-zone simulations.

b. Implementation of the developed interface scheme in a cell-centered finite volume code is straightforward. The interface treatment is fully compatible with the interior numerical discretization assuming the reconstruction accuracy near the interface is of the same order as that of the interior reconstruction. Therefore, loss in accuracy due to grid overlapping is minimized.

c. Comparisons between the conservative Chimera and the original Chimera (i.e., CFD-FASTRAN vs. CFL3D) were carried out side by side. Mass imbalance, shock capturing ability, and convergence properties were examined. The conservative Chimera has consistently performed better than or at least equal to its nonconservative counterpart. It was also shown that the nonconservative Chimera can capture a strong steady shock wave probably because it is zonally conservative.

ACKNOWLEDGMENTS

The work was funded by NASA Ames Research Center under Contract NAS2-13986, with Mr. Pieter Buning being the technical monitor, and the National Science Foundation under Contract DMI-9360558, Dr. Darryl Gorman being the technical monitor. Discussions with Dr. H. Q. Yang, Dr. A. J. Przekwas and A. K. Singhal of CFDRC are greatly appreciated. The use of CFD-FASTRAN from CFDRC and CFL3D from NASA Langley Research Center are gratefully acknowledged.

REFERENCES

1. M. M. Rai, *J. Comput, Phys.* **62,** 472 (1986).
2. M. M. Rai, *J. Comput, Phys.* **66,** 99 (1986).
3. R. W. Walters, J. L. Thomas, and G. F. Switzer, AIAA-86-1063, 1986 (unpublished).
4. G. H. Klopfer and G. A. Molvik, in *Proceedings, AIAA 10th Computational Fluid Dynamics Conference, 1991;* AIAA-91-1601.
5. J. A. Benek, J. L. Steger, and F. C. Dougherty, in *Proceedings, AIAA 6th Computational Fluid Dynamics Conference, 1983;* AIAA-83-1944.
6. J. L. Steger, F. C. Dougherty, and J. A. Benek, "A Chimera Grid Scheme," in *Advances in Grid Generation,* edited by K. N. Ghia, ASME FED, Vol. 5 (ASME, New York, 1985).
7. J. A. Benek, P. G. Buning, and J. L. Steger, in *Proceedings, AIAA 7th Computational Fluid Dynamics Conference, 1985;* AIAA-85-1523.
8. R. L. Meakin and N. E. Suhs, in *Proceedings, AIAA 9th Computational Fluid Dynamics Conference, 1989;* AIAA-89-1996.
9. S. Eberhardt and D. Baganoff, AIAA-85-1542, 1985 (unpublished).
10. Y. J Moon and M-S. Liou, in *Proceedings, AIAA 10th Computational Fluid Dynamics Conference, 1989;* AIAA-89-1980.
11. P. Lax, *Hyperbolic Systems of Conservation Laws and the Mathematical Theory of Shock Waves,* (Society for Industrial and Applied Mathematics, Philadelphia, 1972).
12. M. J. Berger, *SIAM J. Numer. Anal.* **24,** 967 (1987).
13. P. L. Roe, *J. Comput. Phys.* **43,** 357 (1983).
14. B. van Leer, *J. Comput. Phys.* **23,** 276 (1977).
15. CFD Research Corporation, CFDRC Report CFD-GR-9304, 1993 (unpublished).
16. E. Part-Enander and B. Sjogreen, *Comput. & Fluids* **23,** 555 (1994).
17. W. O. Valarezo, C. J. Momonic, and R. J. McGhee, AIAA-91-3332, 1991 (unpublished).